Supporting Information

Mechanistic insights into photocatalysis and over two days of stable H₂ generation in electrocatalysis by a molecular cobalt catalyst immobilized on TiO₂

Nicola Weder,[a] Benjamin Probst,[a] Laurent Sévery,[a] Ricardo J. Fernández-Terán,[a] Jan Beckord,[b] Olivier Blacque,[a] S. David Tilley,[a] Peter Hamm,[a] Jürg Osterwalder[b] and Roger Alberto*[a]

[a]. Department of Chemistry, University of Zurich, Winterthurerstrasse 190, CH-8057 Zurich, Switzerland.

[b]. Department of Physics, University of Zurich, Winterthurerstrasse 190, CH-8057 Zurich, Switzerland.

Tel.: +41 44 635 46 31, Fax: +41 44 635 68 03, Email: ariel@aci.uzh.ch

Table of Contents:

1 Materials and Methods

Analytical Methods

UHPLC-MS: UPLC-MS spectra (low resolution): The column is a ACQUITY UPLC BEH C18 column (1.7 µm, 2.1x50mm). The solvents used were of LCMS grade and composed as following: 0.1% formic acid (A), acetonitrile (B). Gradient: 0 min: 95% A, 5% B, 0.5 min: 95% A, 5% B, 4 min: 100% B, 5 min 100% B.

HR-MS: High-resolution ESI-MS spectra: The samples were dissolved in an appropriate solvent at a concentration of around 1 µmol/mL and measured at a continuous flow of 3 µL/min. The Bruker maXis QTof high-resolution mass spectrometer (Bruker GmbH, Bremen, Germany) was operated in the positive or negative electrospray ionization mode at 4'000 V capillary voltage, -500 V endplate offset, with a N2 nebulizer pressure of 0.8 bar and dry gas flow of 4 L min-1 at 180 °C. MS acquisitions were performed in the mass range from m/z 50 to 2'000 at 20'000 resolution (full width at half maximum) and 1.0 Hz spectra rate. Masses were calibrated prior analysis and below 2 ppm accuracy between m/z 158 and 1450 with a 2 mM solution of sodium formate or between m/z 118 and 2721 with a Fluka electrospray calibration solution (Sigma-Aldrich, Buchs, Switzerland) that has been 100 times diluted with acetonitrile, respectively.

Elemental Analysis: Measurements were performed on a LecoCHNS-932 elemental analyzer at the University of Zürich, Switzerland.

Crystal structure determination: Single-crystal X-ray diffraction data were collected at 160(1) K (using an Oxford liquid-nitrogen Cryostream cooler) on Rigaku Oxford Diffraction diffractometers: a Xcalibur diffractometer with a CCD Ruby detector using the Mo Kα radiation ($\lambda = 0.71073$ Å) from a micro-focus X-ray source for the crystal structure of 4 and a XtaLAB Synergy, Dualflex, Pilatus 200K diffractometer using the Cu Kα radiation ($\lambda = 1.54184$ Å) from a micro-focus sealed X-ray tube for the crystal structures of Co(II)-9 and Co(III)-9. The selected suitable single crystals were mounted using polybutene oil on a flexible loop fixed on a goniometer head and immediately transferred to the diffractometer. Pre-experiment, data collection, data reduction and analytical absorption correction[1] were performed with the program suite CrysAlisPro. Using Olex2,[2] the structures were solved with the SHELXT[3] small molecule structure solution program and refined with the SHELXL2018/3 program package[4] (version 2017/1 or 2018/3) by full-matrix least-squares minimization on F2. PLATON[5] was used to check the results of the X-ray analyses. CCDC 1958070 (for 4), CCDC 1958071 (for (Co(III)-9) and CCDC 1958072 (for Co(II)-9) contain the supplementary crystallographic data for these compounds, and can be obtained free of charge from the Cambridge Crystallographic Data Centre via www.ccdc.cam.ac.uk/Data_request/cif.

X-ray photoelectron spectroscopy: Core level spectra were recorded by X-ray photoelectron spectroscopy (XPS) in a modified VG Escalab 220i XL surface analysis system under ultrahigh vacuum (UHV) conditions ($p \leq 2 \times 10^{-9}$ mbar) at room temperature. The X-ray source was a non-monochromated dual anode X-ray gun emitting Si Kα radiation ($\nu = 1739.5$ eV). The measured Ti 2p3/2 binding energy (not shown) was always within 0.2 eV of the literature value of 459.3 eV[6], so no energy correction was applied. The core level peaks were deconvolved using Gaussian profiles after subtraction of a linear background. The fit was tuned to give the same width for all peaks in a spectrum.

Preparative Methods

Preparation of TiO$_2$ Spin Coating Solution: Titanium oxide nanopowder (TiO$_2$, rutile, high purity, 50 nm, US Research Nanomaterials, Inc.) (2 g) and a solution of ethanol, acetic acid, and water (5:5:1 by volume) (5 mL) were ball-milled with 0.2 mm zirconia balls for 3 h at 500 rpm. After sieving off the zirconia balls, the particles were suspended in 20 ml of ethanol by sonication. To this suspension was added a solution of ethyl cellulose (0.5 g) and terpineol (5 g) in ethanol (25 mL) and the suspension was sonicated for 30 minutes. The ethanol was then removed from the resulting mixture by rotary evaporation. Then, 50 mL of ethanol were added, the mixture was again sonicated for 30 min, and the volatiles again removed. The spin coating solution was made by diluting the resulting viscous white paste with 36 mL of ethanol.

Spin coating of m-TiO$_2$ on FTO-glass: This procedure was adapted from previous literature.[7] An FTO on glass window (FTO TEC 15, Pilkington, Tokyo, Japan) was cut into pieces (1.25 × 2.5 cm) and cleaned by sonicating in acetone, Deconex solution in water (5%), distilled water, and ethanol for 10 min each. After drying in a stream of N$_2$, the pieces were partially covered with Kapton tape on the conductive face, leaving a free area of 1.8 cm^2 . Freshly sonicated spin coating solutions were first applied to the samples, which were then spun at 2000 rpm for 20 s, using an acceleration of 500 rpm per second. After spin coating, the samples were dried on a hot plate at 125 ∘C for 10 min. The spin coating and drying process was repeated 3 times. After the final spin coating, the Kapton tape was removed and the samples sintered in air at 550 ∘C for one hour.

Loading of catalyst on the m-TiO$_2$-coated FTO-glass: The catalyst was anchored by immersion of the plates into an aqueous solution of **6** (100 μM) in 1 mM NaAscO for 12 h. The plates were removed, rinsed with H$_2$O and stored in the dark until their usage.

Experimental Procedures

Electrochemical measurements: All electrochemical measurements were carried out in a 3-electrode cell using a Pt-wire as counter electrode vs. an Ag/AgCl reference. Aqueous saturated KClO$_4$ was used as electrolyte and the solution buffered with acetic acid (50 mM). The pH was adjusted with NaOH. The potential was controlled by a *Bio-Logic SAS, SP-300* potentiostat. Vis-spectra were recorded by a mobile UV-Vis system by *ThorLabs*, with a stabilized tungsten halogen light source (*SLS201/M*) and a compact spectrometer (*CCS200/M*), connected via optical fibers (*400 μm, 0.39NA*). All solutions were freshly prepared and properly degassed prior to each measurements.

Transient Absorption measurements: Transient absorption measurements were recorded on a *LP920-K* laser flash photolysis transient absorption spectrometer using a flash lamp pumped Q-switched Nd:Yag laser (532 nm) as excitation source. Probing of the sample was conducted by a *Xe920* probe lamp (450 W) and an *xP920* pulsing unit module. N$_2$-purged solution samples in 1 cm quartz-cells were used. WRC on TiO$_2$-nanoparticles were measured as a suspension with an amount of loaded particles according to the requested WRC-concentration.

The kinetic traces were normalized and all rate constants were globally fitted within one experiment. The ΔAbs signal was calculated from the time-dependent concentrations of PS$_-$ and Co$_I$, weighted by freely-fit parameters representing their relative contributions to the transient signal.

The kinetic model (Scheme 2 of the manuscript) was evaluated by numerically solving the system of coupled differential equations described therein. In each case, the initial concentrations of PS* and Co^{II} were set according to the experimental conditions, while all other initial concentrations were set to 0. We estimated the initial concentrations of PS*, $[PS^*]_0$, as follows:

$$[PS^*]_0 = \frac{E\lambda}{hcN_A}\left(\frac{1 - 10^{-[PS]_0\varepsilon}}{\pi r^2 L}\right)$$

where we consider the initial concentration of PS ($[PS]_0$), its molar extinction coefficient at the pump wavelength (ε); the energy per pulse (E) and wavelength (λ) of the pump laser, the beam radius at the sample position (r). Given the 90° geometry and collimated beams, we consider also the length of the cuvette (L) and assume a cylindrical excitation profile. N_A is Avogadro's constant, h is Planck's constant and c is the speed of light. Under our experimental conditions, with a 1×1 cm quartz cuvette, r=0.49 cm, E=68 mJ, λ=532 nm, and ε≈810 M_{-1} cm$_{-1}$. For the WRC-excess conditions, $[PS]_0$=50 μM, yielding $[PS_*]_0$≈35.5 μM. For the WRC-deficient conditions, $[PS]_0$=300 μM, yielding $[PS_*]_0$≈170 μM. All data analysis was performed in home-made scripts in MATLAB r2019a.

Fig. S5 provides an example of the time-dependent concentrations obtained from the fits to the kinetic traces of the WRC-excess experiment in solution.
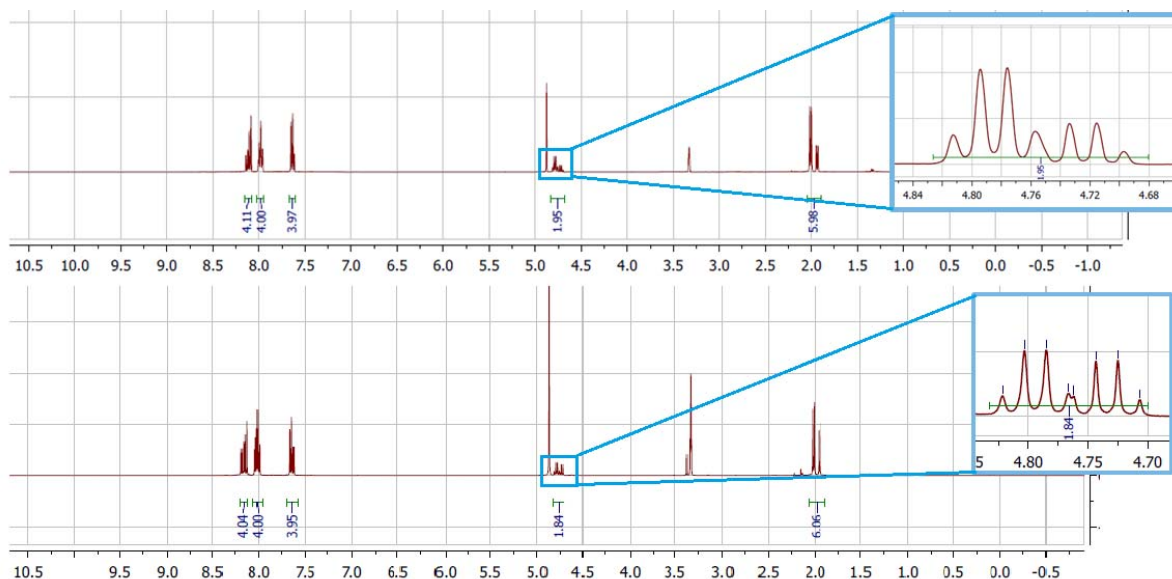
2 Deuterium experiments with dimethylpyrphyrin

Figure S1: ^{1}HNMR spectra of compound **3** (top) and after deprotonation of **3** by KO*t*Bu and quenching after 1 h by methanol-d$_4$ (bottom). The signal at 4.75 ppm corresponds to the proton at the bridging position, which was intended to be deprotonated. However, the small decrease of the integral hints towards a rather high pK$_A$ of the respective protons, thus, slow deprotonation. But the deprotonation appeared to proceed during the ongoing nucleophilic addition to the diethylvinyl phosphonate.

3 Characterization of 6@NP-TiO₂
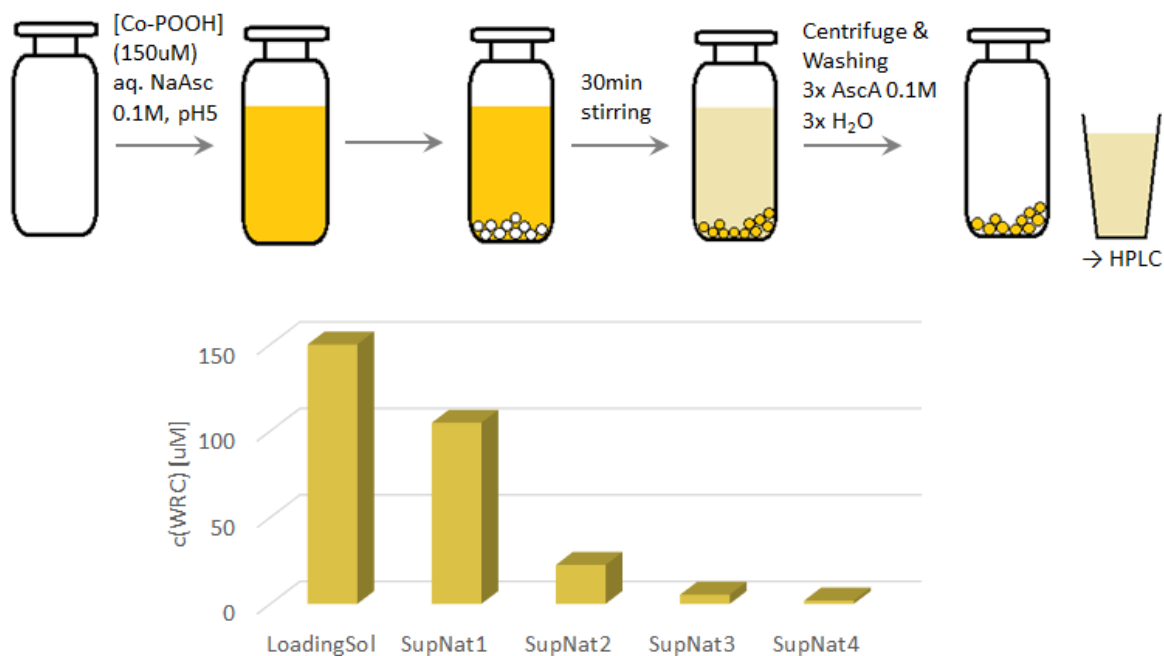
Figure S2: Footprint determination of **6@NP-TiO₂**: the catalyst was dissolved in aqueous ascorbic acid, titrated with NaOH to pH5, and an exact amount of P25-TiO₂ nanoparticles (purchased from *Sigma Aldrich*) was added and stirred for 30 minutes. The particles were centrifuged off and an exact amount (90 % of the original volume) of the supernatant removed and analyzed by HPLC (SupNat1). An equivalent amount of pure H₂O to the removed aliquot was added to the suspension and after the particles were centrifuged off from new, the 2nd supernatant (SupNat2) was analyzed. This procedure was repeated two more times until no traceable WRC was detected in the supernatant anymore. The footprint of the WRC was calculated as the difference of the WRC found in all supernatants and the originally inserted amount, divided by the known BET-surface of the applied TiO₂-particle amount.
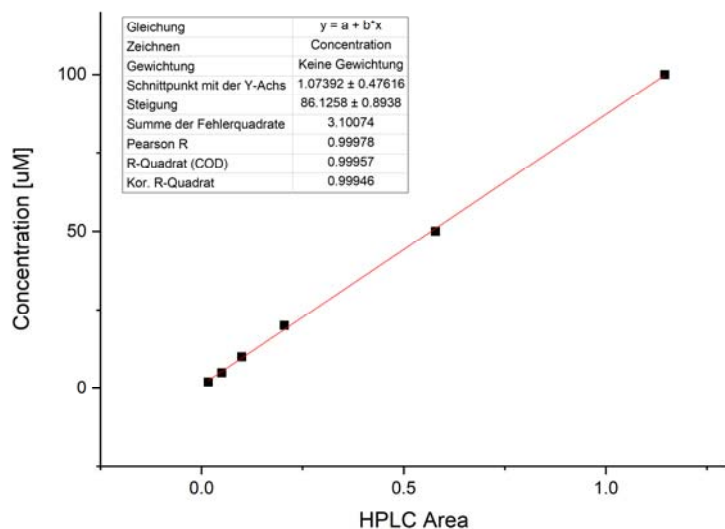
Gleichung	y = a + b*x
Zeichnen	Concentration
Gewichtung	Keine Gewichtung
Schnittpunkt mit der Y-Achs	1.07392 ± 0.47616
Steigung	86.1258 ± 0.8938
Summe der Fehlerquadrate	3.10074
Pearson R	0.99978
R-Quadrat (COD)	0.99957
Kor. R-Quadrat	0.99946

Figure S3: WRC-concentration (**6** in 0.1M NaAscO) to HPLC-Area Regression curve.
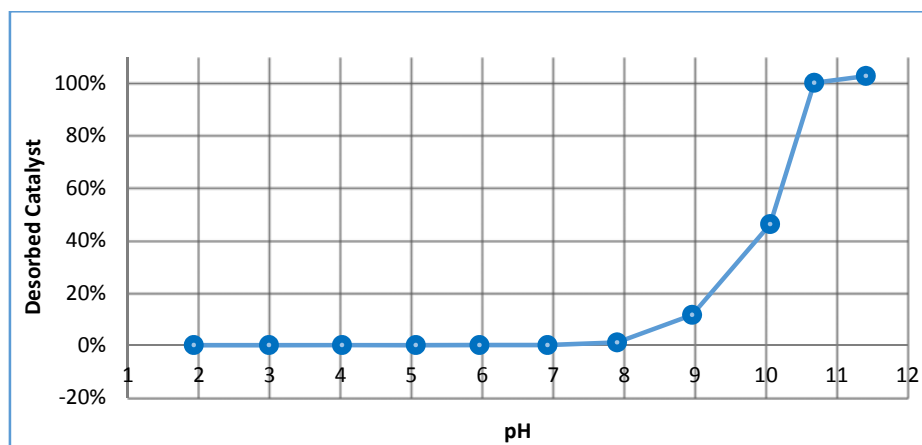
Figure S4: pH stability of the immobilized catalyst. Loaded particles were weighted exactly, suspended in H_2O and the pH adjusted by means of much diluted NaOH. After an equilibration time of 30 minutes, the particles were centrifuged off and the desorbed catalyst in the supernatant quantitatively analyzed by HPLC according to the method discussed above.

4   Kinetic Measurments
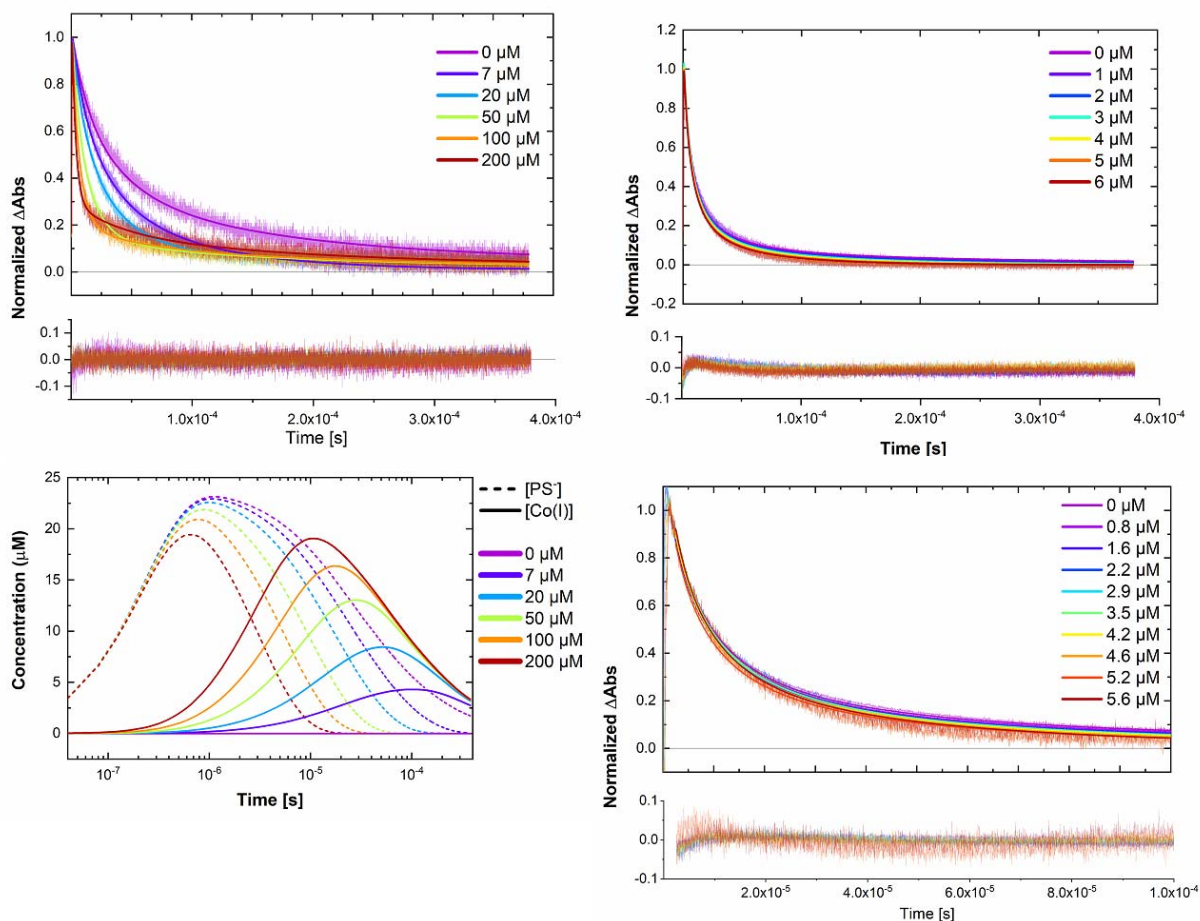
Figure S5: Kinetic absorption (510 nm) incl. residuals of WRC excess, in solution (top left), WRC deficient, in solution (top right) and WRC deficient on particles (bottom right). Measurement conditions correspond to the ones described in Figure 3. The concentration profile (bottom left) correspond to the global fit under WRC-excess conditions.

5 Photocatalysis

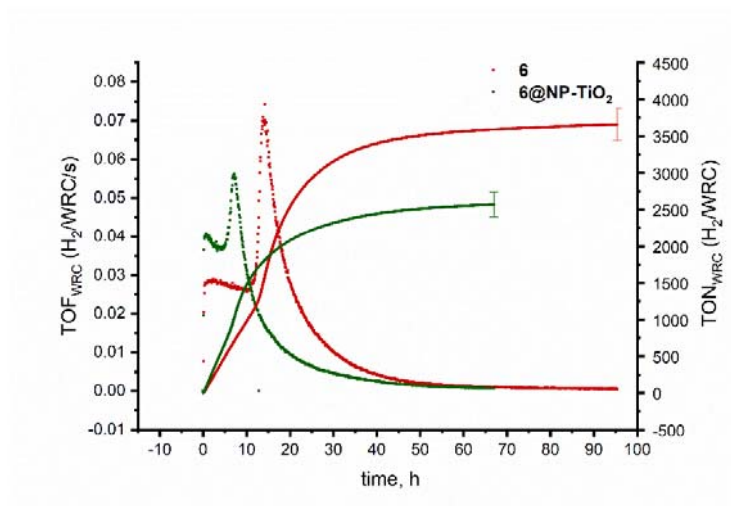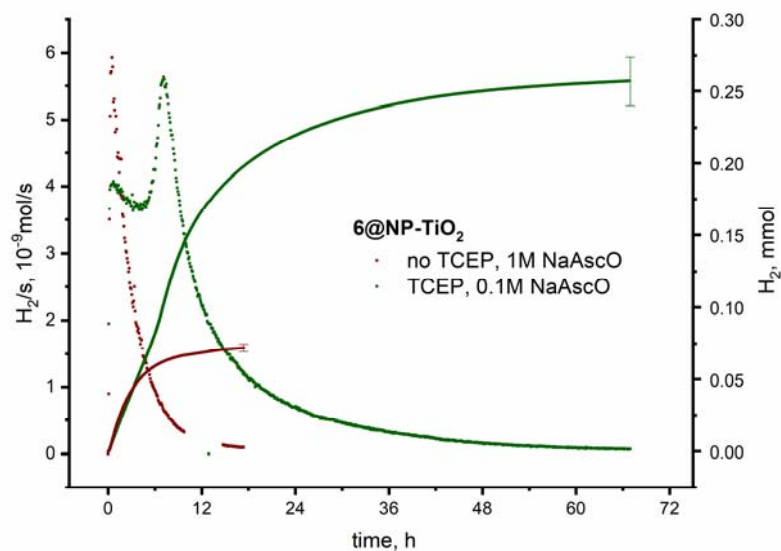The setup of photocatalytic measurements is described elsewhere.[8]

Figure S6: Comparison the H_2-evolution traces of two samples containing 500 μM PS, 0.1 M NaAscO, 0.1 M TCEP and red: 10 μM **6**, and green: 10 μM of **6@NP-TiO$_2$**. The dots correspond to the turnover frequency (TOF, left y-axes) whereas the straight lines represent the turnovernumbers (TON, right y-axes).
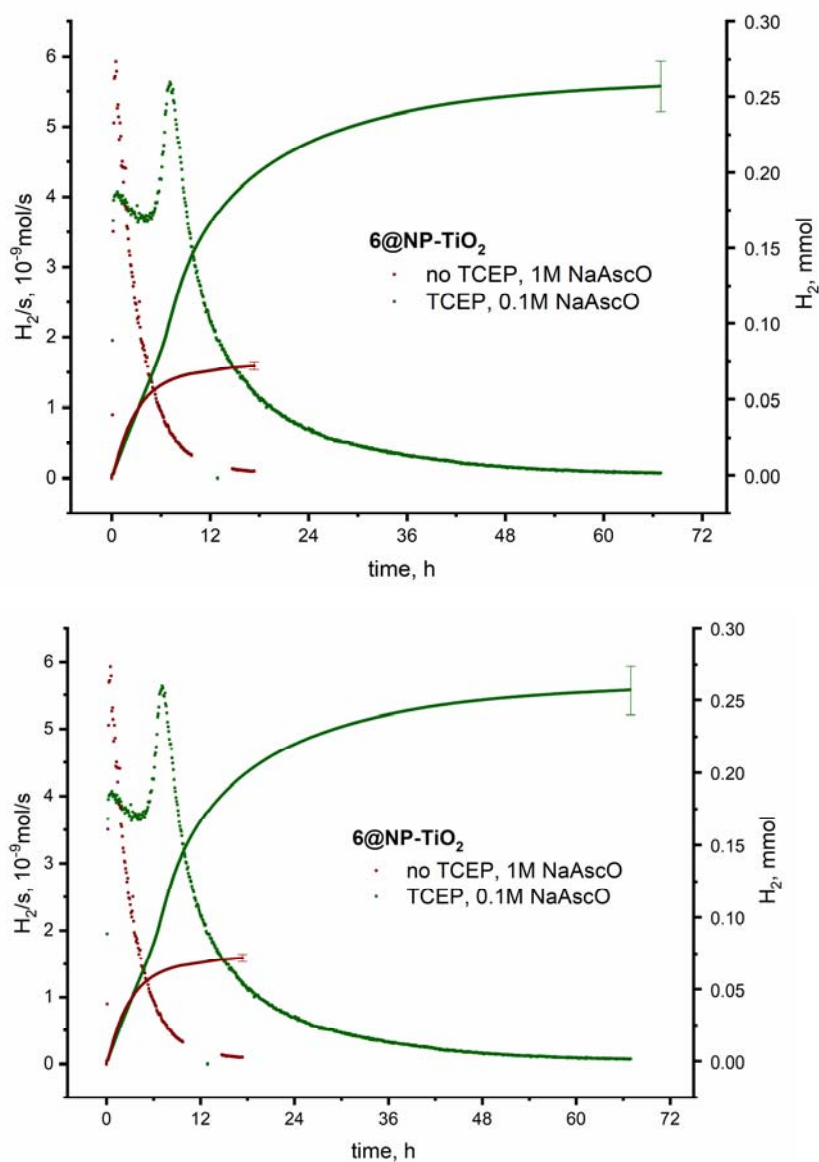
Figure S7: Influence of TCEP on the catalytic H_2-evolution trace. The experimental conditions are, green: 500 μM PS, 0.1 M NaAscO, 0.1 M TCEP, 10 μM of WRC, and red: 500 μM PS, 1.0 M NaAscO, and 10 μM of WRC. The WRC of the different experiments is (from top to bottom): **8**, **6** and **6@NP-TiO₂**. The two subsequent production rate maxima vanish in the measurements without TCEP, hence, can be attributed to formation of a TCEP adduct. However, the amount of evolved H_2 is less than half of the volume of the case with TCEP. This effect is due to back electron transfer from the reduced PS to dehydroascorbic acid (DHA), the reaction product of ascorbate oxidation.
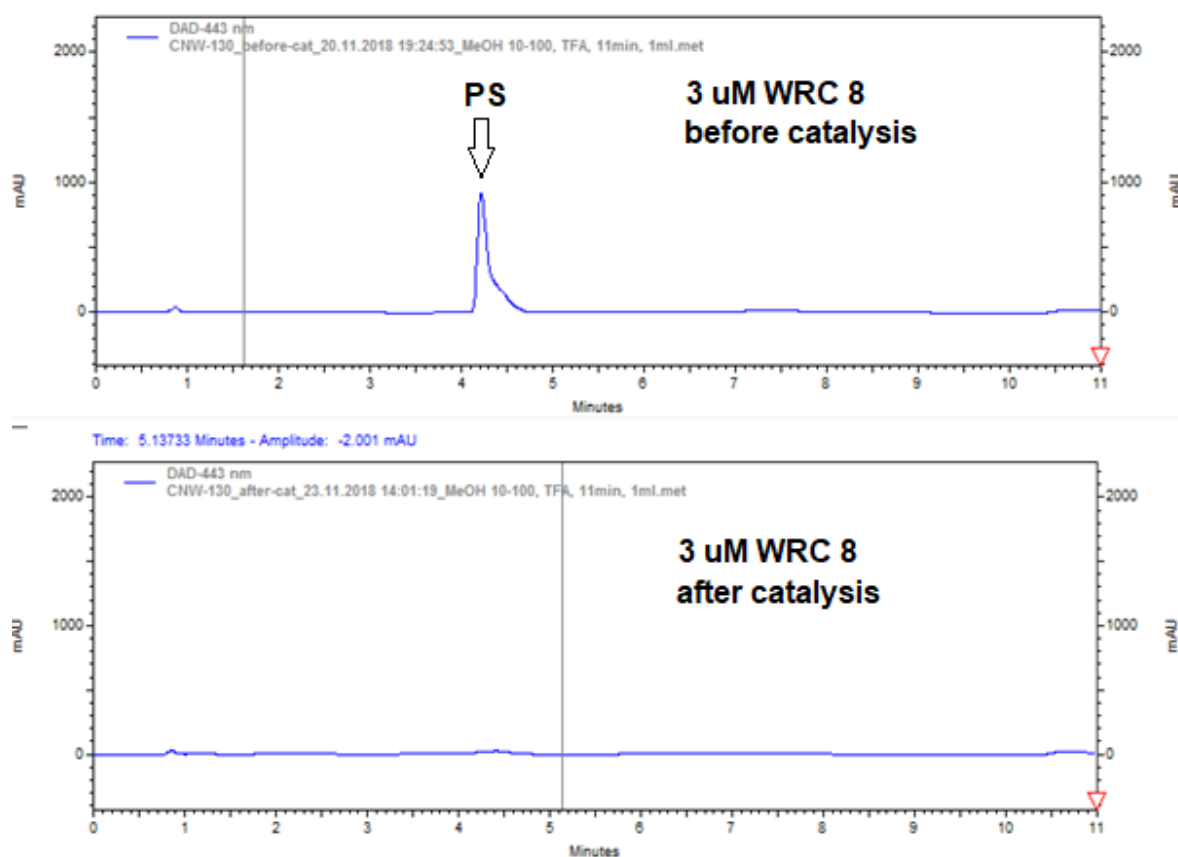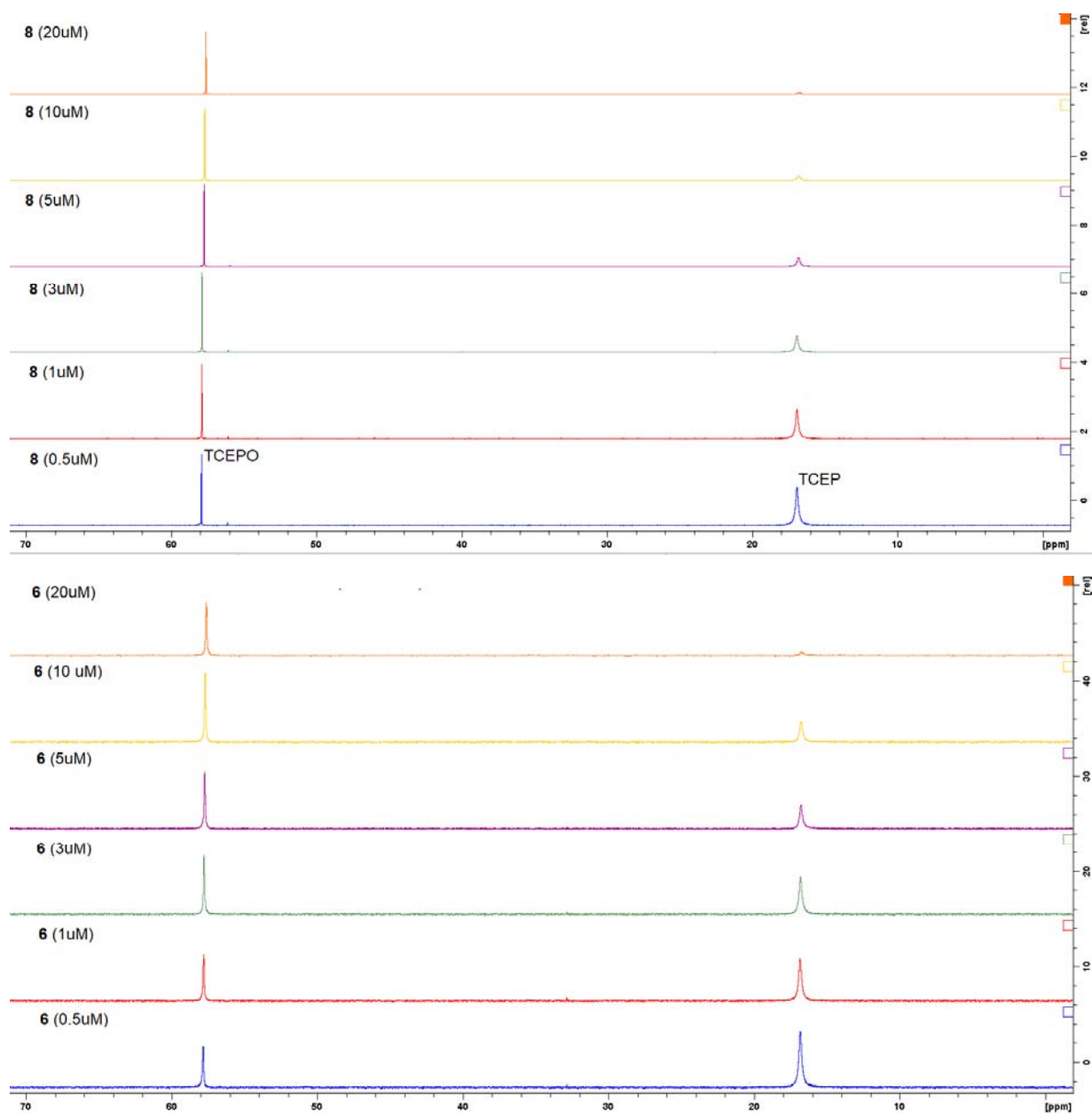
Figure S8: HPLC-traces at 445 nm of the catalytic solution before (tope) and after (bottom) catalysis (initial conditions of catalysis: 500 µM [Ru(bipy)$_3$]Cl$_2$, 3 µM **8**, 0.1 M NaAscO and 0.1 TCEP, pH 5.. Retention time of 4.3 minutes corresponds to the photosensitizer (PS). Full degradation of the PS as the stability limiting factor of photocatalysis was confirmed by this measurement.
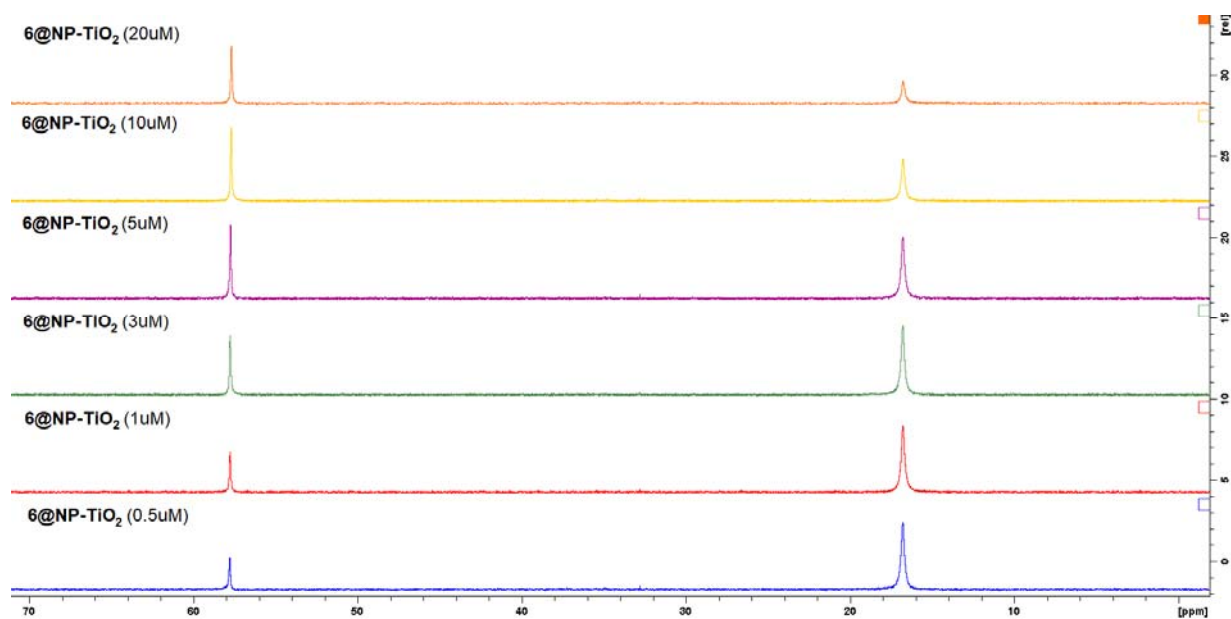
Figure S9: ^{13}P NMR after the respective photocatalytic experiments of **8** (top), **6** (middle) and **6@NP-TiO$_2$** (bottom). The signal at 16.4 ppm corresponds to non-consumed TCEP, the signal of TCEPO is shifted to 57.9 ppm. Especially at high concentrations of **6** and **8** full TCEP consumption limits photocatalysis. With decreasing WRC concentration the PS was completely degenerated before the TCEP was fully oxidized.
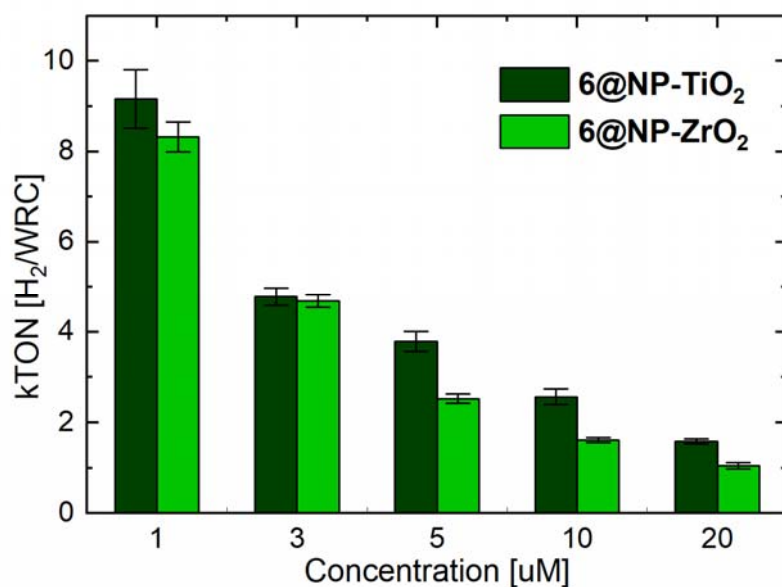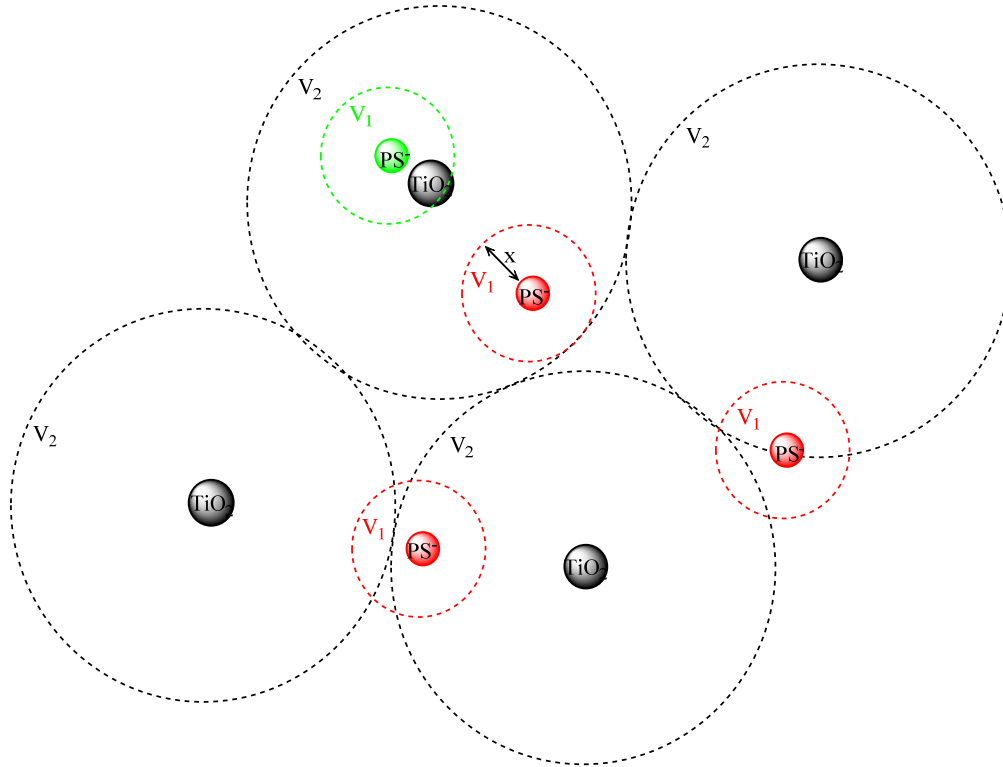

Figure S10: TONs determined from photocatalysis (in H$_2$ WRC^{-1}) of **6@NP-TiO$_2$** (dark green) and **6@NP-ZrO$_2$** (bright green). Both experiments contained 500 μM [Ru(bipy)$_3$]$^{2+}$, 0.1 M NaAscO and 0.1 M TCEP as electron relay and sacrificial electron donor, respectively.

$$D(PS) = \frac{RT}{6\pi r \eta N_A} = 4.018 * \frac{10^{-10} m^2}{s}; D = Diffusioncoefficient$$

$$R = 8.3145 kg * \frac{m^2}{s^2 mol * K}; T = 298.15K; r = 6.1\text{Å, (lit. value}^9) \; \eta_{H_2O} = 0.891 * \frac{10^{-3} Pa}{s}$$

$$\Delta x = (\Delta t * 2D)^{\frac{1}{2}}$$

$\Delta t = 30 \mu s$ (from concentration profile, Figure 2)

$$V_1 = \frac{4}{3}\pi * x^3 = 1.56 * 10^{-14} ml \; (= V_1)$$

For catalysis with 5 μM WRC on particles:

$$N_{particles} = 1.3 * 10^{14} \text{ particles}$$

$$\frac{V_{occupied}}{particles} = \frac{10 ml}{1.3 * 10^{14}} = 7.65 * 10^{-14} ml \; (= V_2)$$

$$\frac{V_1}{V_2} = 20\%$$

Figure S11: Schematic illustration of the diffusion distance (x) or the "points of accessibility" of the reduced PS within 30 μs (V_1) compared to the volume occupied by one TiO_2 nanoparticle (V_2) in case of

equal distribution of the particles in the suspension. Only if a particle lies within V_1 (green, broken line), there is the possibility of productive oxidation of PS^- (given the correct diffusion direction of the PS^- and the redox reaction actually taking place), in any other case (red, broken lines), the PS^- is oxidized via recombination or decomposition.
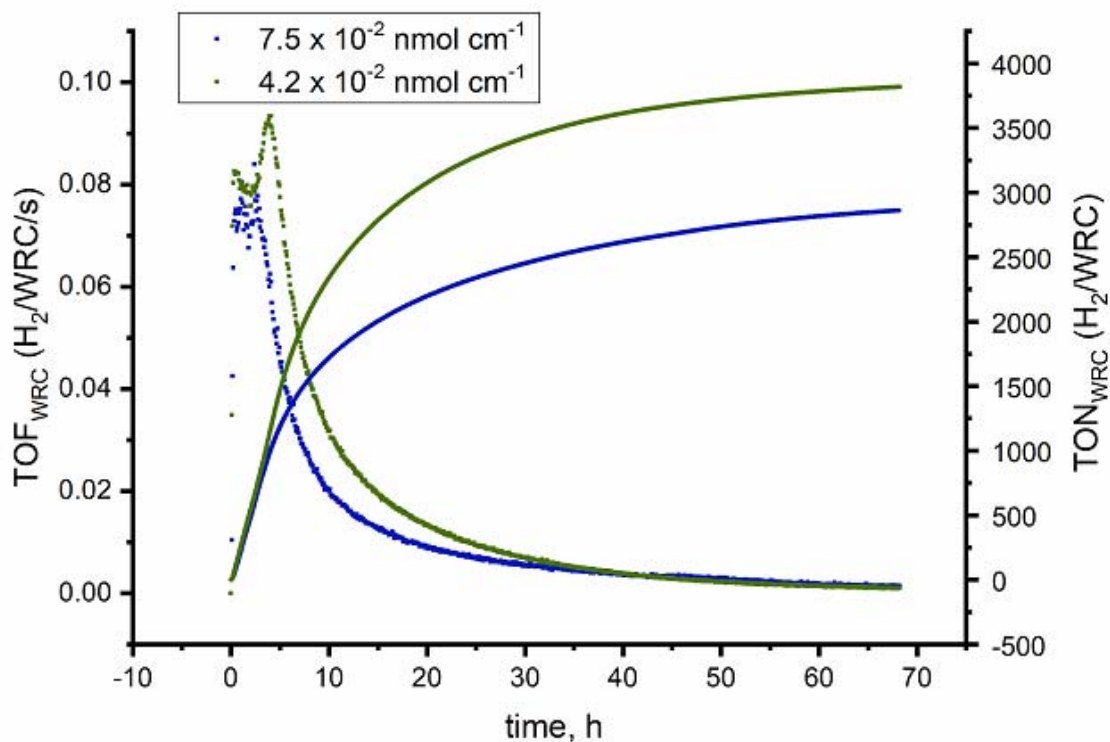

Figure S12: Footprint: Comparison of the H_2-evolution traces of two samples containing 500 μM PS, 0.1 M NaAsc, 0.1 M TCEP and 5 μM **6@NP-TiO₂**, each, but blue: loading density of 7.5 x 10^{-2} nmol cm^{-2} (footprint of 2.21 nm^2) and green: loading density of 4.2 x 10^{-2} nmol cm^{-2} (footprint of 3.96 nm₂). The wider distribution of the WRC in case of the lower loading density makes it more accessible for the reduced PS, therefore, increased TOF and TON.
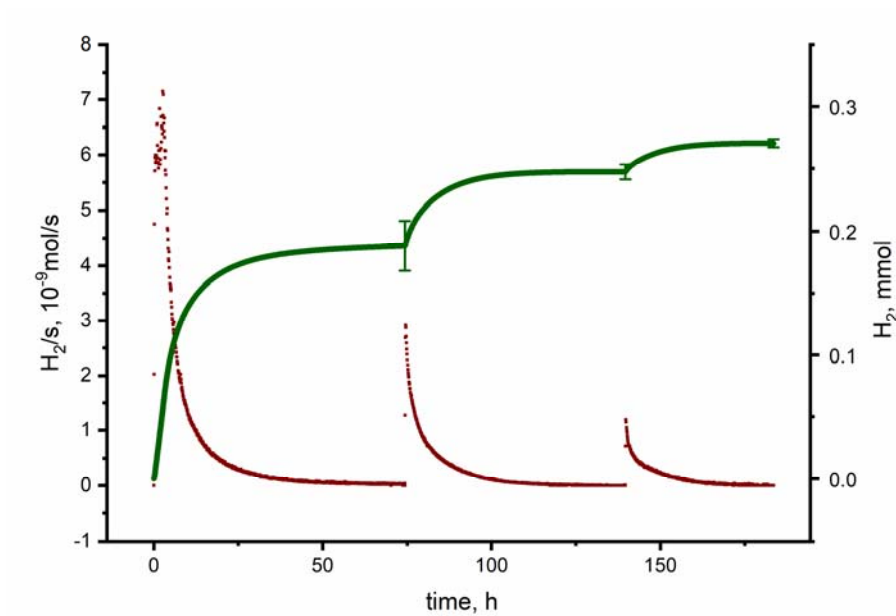
Figure S13: Recycle experiments of **6@NP-TiO$_2$**. Conditions for 1st catalysis: 500 µM PS , 5 µM WRC, 0.1 M NaAscO, 0.1 M TCEP, pH 5. The NPs were separated from the solution by centrifugation after cessation of H$_2$ formation, washed with water (3x) and dried. An equivalent mass of recycled NPs to the first run was suspended in a fresh solution containing the same amounts of PS, NaAscO and TCEP. This procedure was repeated one more time.
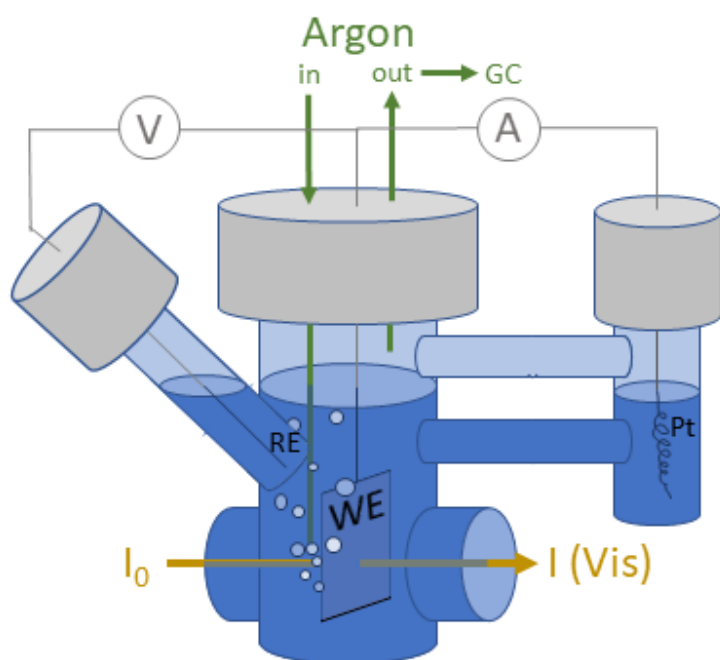
6 Electrocatalysis

Figure S14: Electrochemical measurements were carried out in a custom made three electrode cell. The grey plate represents the m-TiO$_2$-coated FTO-glass, which is loaded with **6** as active catalyst. RE is the reference electrode (Ag/AgCl) and the Pt-wire represents the counter electrode. Two opposite glass windows on both sides of the working electrode allowed for measuring the Vis-absorption (yellow arrow) of the adsorbed catalyst dependent on the applied potential. Gas in- and outlet (brown tubes) were installed to degas the solution as well as the outlet was used to measure evolved H$_2$ during long-term chronoamperometric measurements.
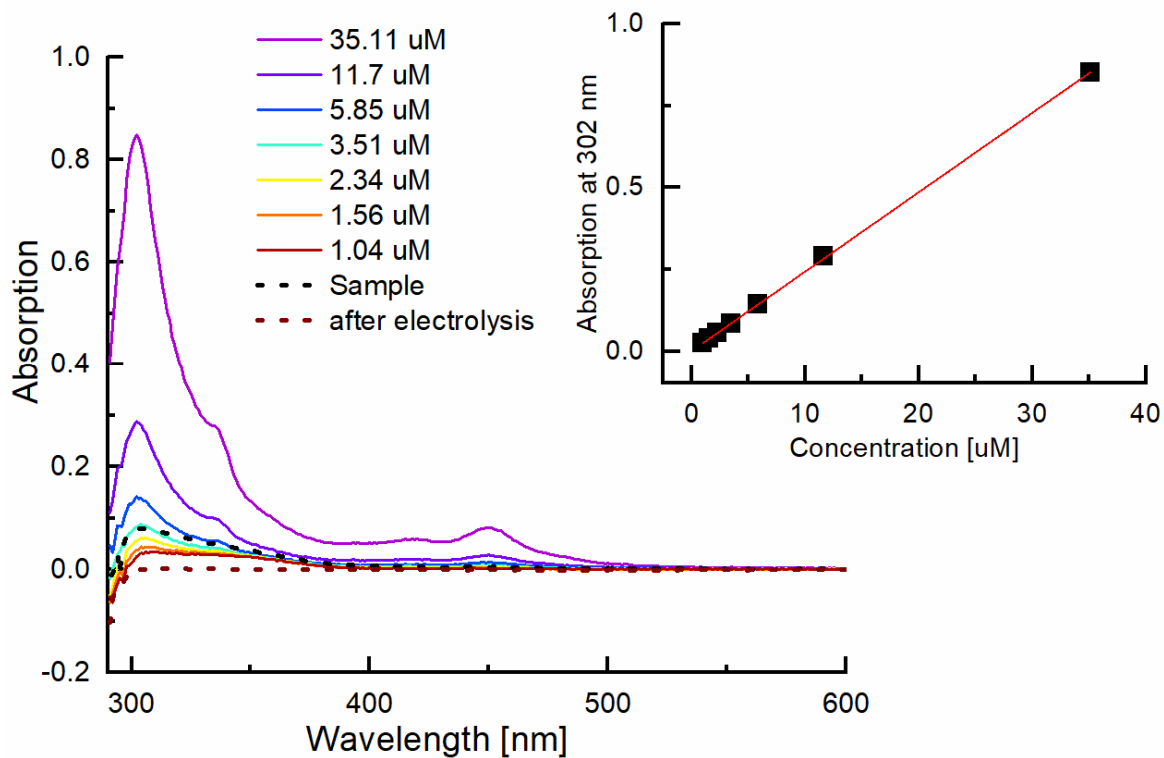
Figure S15: Absorption spectra of 6 in aq. 0.5 M Na_2HPO_4 solution with 1 mM NaAscO at pH 7. The linear regression of the absorption at 302 nm is shown in the inset. The black spectrum corresponds to the measurement of the solution after immersion of a loaded *m*-TiO_2-coated FTO-glassplate into the phosphate solution.
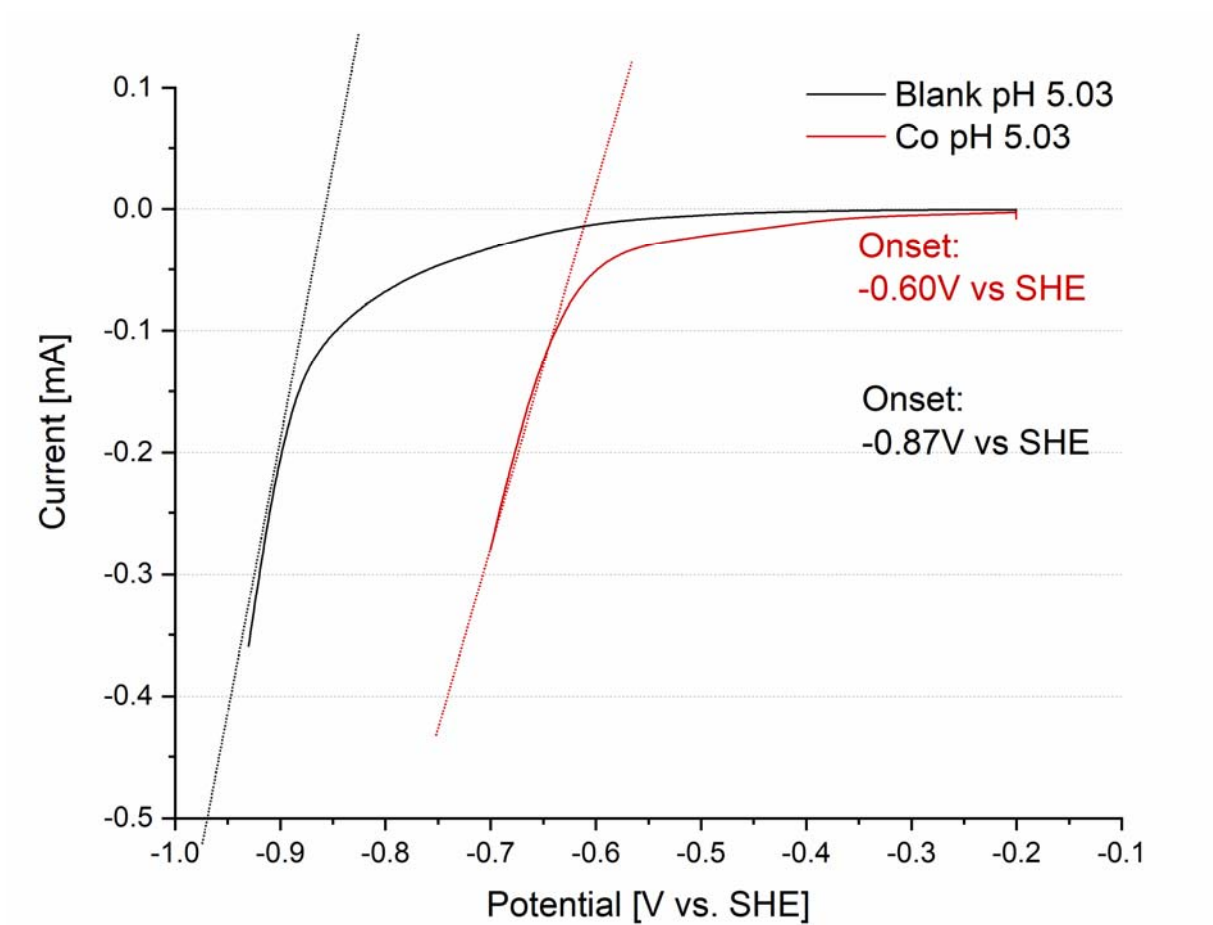
Figure S16: LSV measurement to determine the onset potential by linear extrapolation method, as indicated by the dotted lines. Conditions: $KClO_4$ (aq. sat.), acetic acid (50 mM) at pH 5. The working electrode was **6@*m*-TiO$_2$** (red trace) or **11@*m*-TiO$_2$** (black trace), using a Pt wire as counter electrode and Ag/AgCl as reference. The onset potential is the point of intersection of the extrapolation of the linear part of the LSV trace and the x-axes.
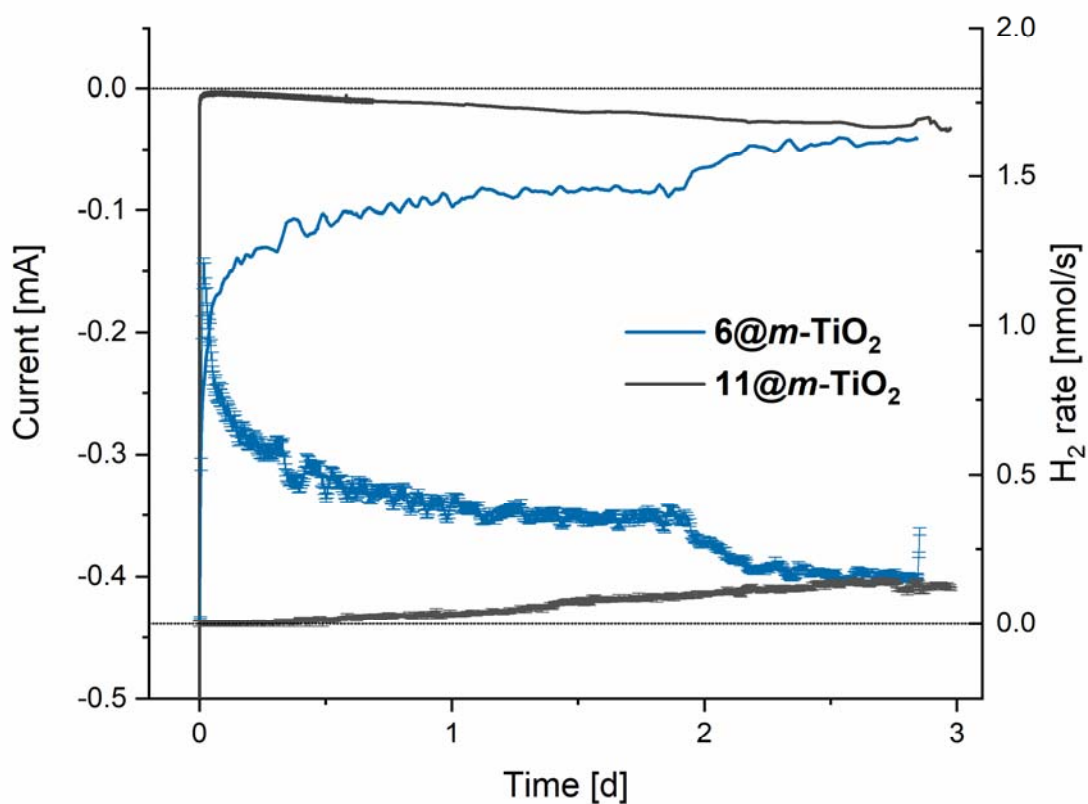
Figure S17: CA experiments of blue: **6@*m*-TiO₂** and grey: **11@*m*-TiO₂** in aq. sat. KClO₄, 50 mM acetic acid at pH 5. The increasing current and H_2-formation of the zinc-blank is attributed to the slow reduction of the substrate to Ti^{III}-doped TiO_2, a known proton reduction catalyst without need of any co-catalyst.[10] The blue to dark-blue coloration of the mesoporous TiO_2 film, which was observed after prolonged exposure to reducing conditions, is another hint for this phenomenon as this color is multiply reported in literature.[11] The blue data are depicted "as obtained" in this figure, however, corrected by the blank current and $-H_2$-rate for further analysis (see Fig. 6 in the main text).

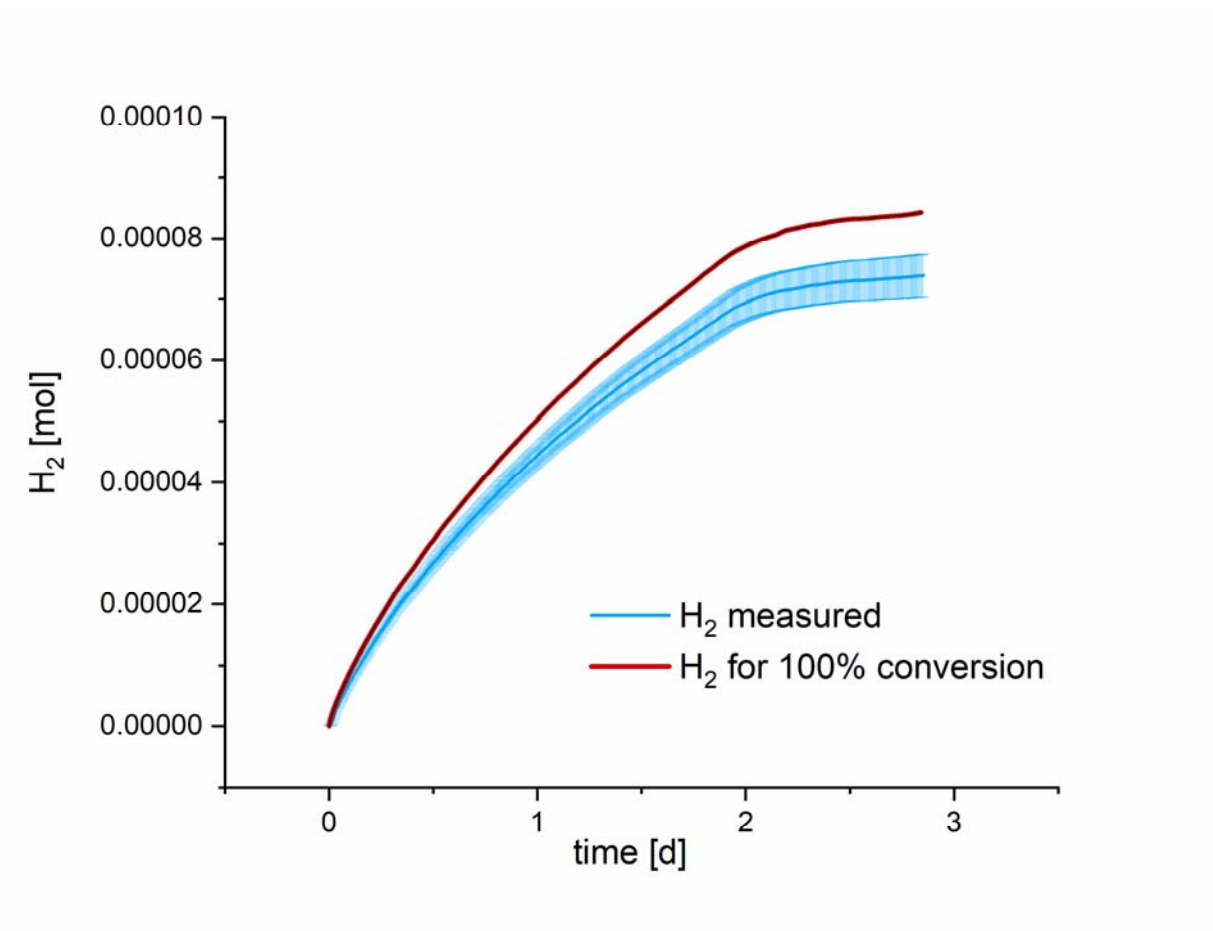**Figure S18**: H_2-evolution trace (blue line) and current trace calculated to the theoretical amount of H_2-formation at 100 % conversion (red line,) of chronoamperometric measurement of **6@*m*-TiO₂** at –0.65 V in aq. sat. KClO₄, 50 mM acetic acid at pH 5. The 100 % conversion amount is calculated according to:

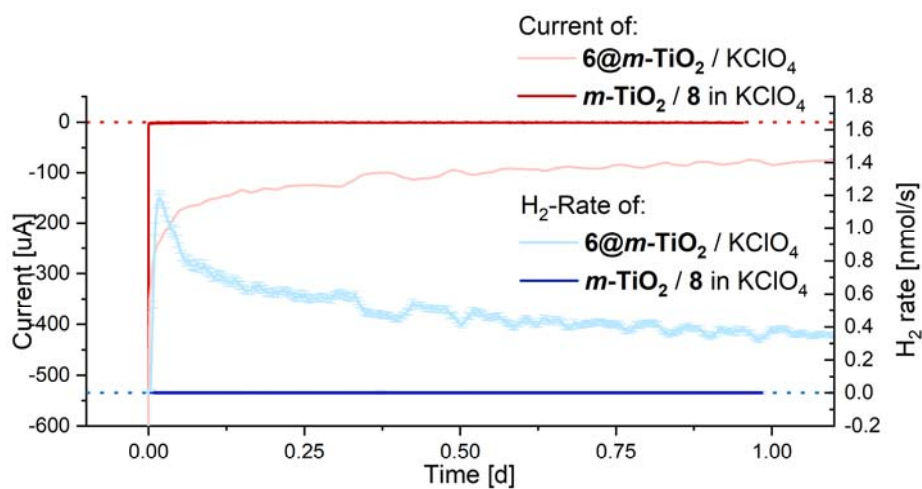$$H_2\left[\frac{mol}{s}\right] = \frac{I[A]}{2 * 96485\left(s * \frac{A}{mol}\right)}$$

Figure S19: CA measurements to exclude catalytic activity of desorbed catalyst. Red corresponds to current, blue to H_2-formation. Conditions (non-transparent): electrolyte additionally contained **8** (0.3 μM, corresponding to the theoretical WRC concentration at full desorption from the working electrode). The transparent data are given as comparison and correspond to the data provided in Figure 6. The potential was set to –0.65 V vs. SHE in both experiments. The non-transparent data clearly indicate no catalytic activity of dissolved WRC.
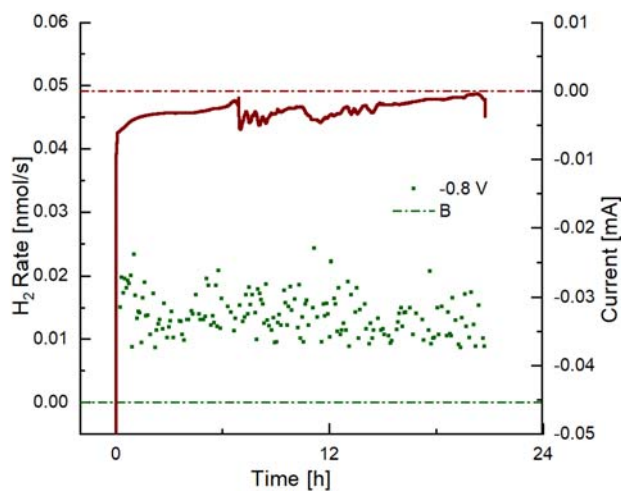

Figure S20: CA measurement at –0.6 V vs. SHE. Traces of H_2 (green dots) detected, confirming the onset-potential of –0.6 V vs. SHE.

22
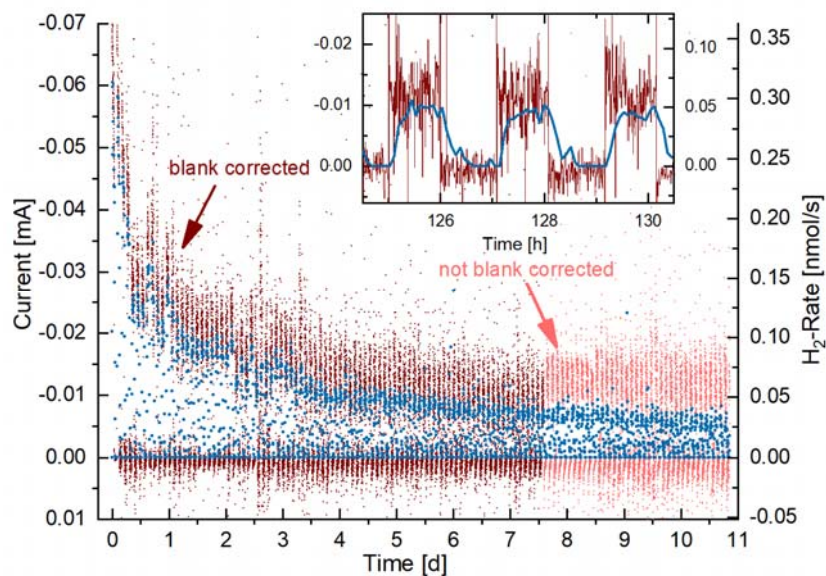
Figure S21: CA measurements with alternating potential. The current is given in red (left y-axis) and H_2-formation in blue (right y-axes). Conditions: **6@*m*-TiO₂** as WE, acetic acid (50 mM) in aq. sat. KClO₄. The potential was switched between –0.65 V vs. SHE (60min) and +0.2 V (65min). The data during the first 7.5 days were corrected by a corresponding blank measurement applying the Zn-complex **11@*m*-TiO₂**. At later times, the data are not corrected, however, the difference is marginal. Electrocatalysis is re-initiated after every equilibration phase at +0.2 V vs. SHE, and H_2-formation follows the same trend (see inset).

7 Crystallographic data

Table S1: Crystal data and structure refinement for compound 4

|	
Empirical formula	$C_{36}H_{46}N_4O_6P_2$
Formula weight	692.71
Temperature/K	160(1)
Crystal system	triclinic
Space group	P-1
a/Å	9.4370(2)
b/Å	10.4908(3)
c/Å	18.5143(4)
α/°	96.9776(19)
β/°	99.2858(19)
γ/°	104.161(2)
Volume/Å^3	1728.96(7)
Z	2
ρcalcg/cm^3	1.331
μ/mm^{-1}	0.178
F(000)	736.0
Crystal size/mm^3	0.45 × 0.36 × 0.24
Radiation	MoKα ($\lambda = 0.71073$)
2Θ range for data collection/°	5.2 to 50.7
Index ranges	-11 ≤ h ≤ 11, -12 ≤ k ≤ 12, -22 ≤ l ≤ 22
Reflections collected	34712
Independent reflections	6339 [$R_{int} = 0.0251$, $R_{sigma} = 0.0171$]
Data/restraints/parameters	6339/0/439
Goodness-of-fit on F^2	1.018
Final R indexes [I>=2σ (I)]	$R_1 = 0.0387$, $wR_2 = 0.0937$
Final R indexes [all data]	$R_1 = 0.0439$, $wR_2 = 0.0974$
Largest diff. peak/hole / e Å^{-3}	1.02/-0.40
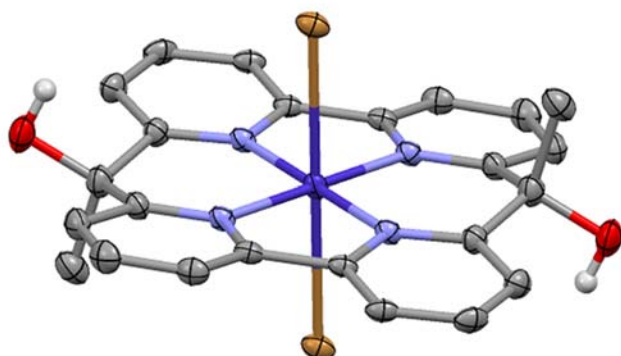
Figure S22: Crystal structure of compound **9** with cobalt in +2 oxidation state. Selected H-atoms and solvent molecules were omitted for clarity. 30 % thermal ellipsoid probability level. Color code: grey (C), white (H), brown (Br), purple (Co), bright blue (N), red (O).

Table S2: Crystal data and structure refinement for Co(II)-9

|	
Empirical formula	$C_{26}H_{28}Br_2CoN_4O_4$
Formula weight	679.27
Temperature/K	160(1)
Crystal system	monoclinic
Space group	P21/n
a/Å	8.0833(1)
b/Å	11.8214(1)
c/Å	13.6272(1)
α/°	90
β/°	95.751(1)
γ/°	90
Volume/Å^3	1295.61(2)
Z	2
ρcalcg/cm^3	1.741
μ/mm^{-1}	9.148
F(000)	682.0
Crystal size/mm^3	0.17 × 0.03 × 0.02
Radiation	CuKα (λ = 1.54184)
2Θ range for data collection/°	9.926 to 149.002
Index ranges	-10 ≤ h ≤ 10, -14 ≤ k ≤ 14, -15 ≤ l ≤ 17
Reflections collected	26383
Independent reflections	2644 [R_{int} = 0.0344, R_{sigma} = 0.0174]
Data/restraints/parameters	2644/2/177
Goodness-of-fit on F2	1.081
Final R indexes [I>=2σ (I)]	R_1 = 0.0345, wR_2 = 0.0928
Final R indexes [all data]	R_1 = 0.0365, wR_2 = 0.0942
Largest diff. peak/hole / e Å^{-3}	0.95/-0.49
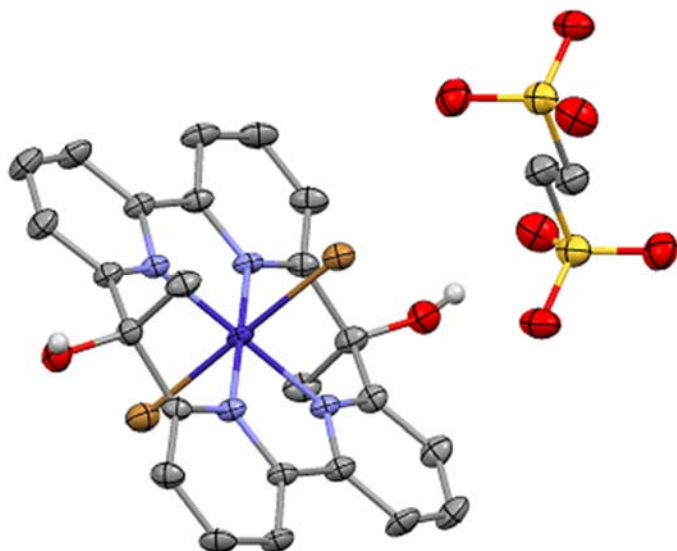
Figure S23: Crystal structure of compound **9** with cobalt in +3 oxidation state. The unit cell includes one 1,2-ethanedisulfonate counter-ion $[C_2H_4S_2O_6]_{2-}$ per two complex molecules. Selected H-atoms and solvent molecules were omitted for clarity. 50 % thermal ellipsoid probability level. Color code: grey (C), white (H), brown (Br), purple (Co), bright blue (N), red (O), yellow (S).

Table S3: Crystal data and structure refinement for Co(III)-9

Empirical formula	$C_{27}H_{30}Br_2CoN_4O_7S_2$
Formula weight	805.42
Temperature/K	160(1)
Crystal system	triclinic
Space group	P-1
a/Å	8.1545(3)
b/Å	11.7917(5)
c/Å	16.3115(4)
α/°	107.981(3)
β/°	96.136(3)
γ/°	103.720(3)
Volume/Å^3	1421.47(9)
Z	2
ρcalcg/cm^3	1.882
μ/mm^{-1}	9.878
F(000)	810.0
Crystal size/mm^3	0.11 × 0.03 × 0.02
Radiation	CuKα (λ = 1.54184)
2Θ range for data collection/°	5.808 to 149.008
Index ranges	$-10 \le h \le 10$, $-14 \le k \le 13$, $-13 \le l \le 20$
Reflections collected	21345
Independent reflections	5801 [R_{int} = 0.0394, R_{sigma} = 0.0366]
Data/restraints/parameters	5801/2/400
Goodness-of-fit on F2	1.030
Final R indexes [I>=2σ (I)]	R_1 = 0.0412, wR_2 = 0.1032
Final R indexes [all data]	R_1 = 0.0499, wR_2 = 0.1077
Largest diff. peak/hole / e Å^{-3}	1.29/-0.72

8 References

1.	Clark, R. C.; Reid, J. S., The analytical calculation of absorption in multifaceted crystals. *Acta Cryst.* **1995,** *51*, 11.
2.	Dolomanov, O. V.; Bourhis, L. J.; Gildea, R. J.; Howard, J. A. K.; Puschmann, H., OLEX2: a complete structure solution, refinement and analysis program. *Journal of applied crystallography* **2009,** *42*, 3.
3.	Sheldrick, G. M., SHELXT - Integrated space-group and crystal-structure determination. *Acta Cryst.* **2015,** *71*, 6.
4.	Sheldrick, G. M., Crystal structure refinement with SHELXL. *Acta Cryst.* **2015,** *71*, 6.
5.	Spek, A. L., Structure validation in chemical crystallography. *Acta Cryst.* **2009,** *65*, 8.
6.	Diebold, U.; Madey, T. E., TiO2 by XPS. *Surf Sci Spectra* **1998,** *4*, 227-231.
7.	Sévery, L.; Siol, S.; Tilley, S., Design of Molecular Water Oxidation Catalysts Stabilized by Ultrathin Inorganic Overlayers—Is Active Site Protection Necessary? *Inorganics* **2018,** *6* (4), 105.
8.	Joliat-Wick, E.; Weder, N.; Klose, D.; Bachmann, C.; Spingler, B.; Probst, B.; Alberto, R., Light-Induced H2 Evolution with a Macrocyclic Cobalt Diketo-Pyrphyrin as a Proton-Reducing Catalyst. *Inorg Chem* **2018,** *57* (3), 1651-1655.
9.	Marti, A. A.; Colon, J. L., Photophysical characterization of the interactions among tris(2,2'-bipyridyl)ruthenium(II) complexes ion-exchanged within zirconium phosphate. *Inorg Chem* **2010,** *49* (16), 7298-303.
10.	(a) Zhang, Z.; Hedhili, M. N.; Zhu, H.; Wang, P., Electrochemical reduction induced self-doping of Ti3+ for efficient water splitting performance on TiO2 based photoelectrodes. *Physical chemistry chemical physics : PCCP* **2013,** *15* (37), 15637-44; (b) Liu, N.; Schneider, C.; Freitag, D.; Hartmann, M.; Venkatesan, U.; Muller, J.; Spiecker, E.; Schmuki, P., Black TiO2 nanotubes: cocatalyst-free open-circuit hydrogen generation. *Nano letters* **2014,** *14* (6), 3309-13.
11.	(a) Zhao, Z.; Tan, H.; Zhao, H.; Lv, Y.; Zhou, L. J.; Song, Y.; Sun, Z., Reduced TiO2 rutile nanorods with well-defined facets and their visible-light photocatalytic activity. *Chemical communications* **2014,** *50* (21), 2755-7; (b) Lu, H.; Zhao, B.; Pan, R.; Yao, J.; Qiu, J.; Luo, L.; Liu, Y., Safe and facile hydrogenation of commercial Degussa P25 at room temperature with enhanced photocatalytic activity. *RSC Adv.* **2014,** *4* (3), 1128-1132; (c) Wang, G.; Wang, H.; Ling, Y.; Tang, Y.; Yang, X.; Fitzmorris, R. C.; Wang, C.; Zhang, J. Z.; Li, Y., Hydrogen-treated TiO2 nanowire arrays for photoelectrochemical water splitting. *Nano letters* **2011,** *11* (7), 3026-33.